Water Resources Research

RESEARCH ARTICLE
10.1029/2020WR028331

Potential of Hydraulic Tomography in Identifying Boundary Conditions of Groundwater Basins

Fei Liu[1,2], Tian-Chyi Jim Yeh[2,3], Yu-Li Wang[2], Xianfang Song[4], Xiaohui Lei[5], Jet-Chau Wen[6,7], Wenke Wang[8], and Yonghong Hao[3]

[1]School of Water Conservancy and Hydropower, Hebei University of Engineering, Handan, China, [2]Department of Hydrology and Atmospheric Sciences, University of Arizona, Tucson, AZ, USA, [3]Tianjin Key Laboratory of Water Resources and Environment, Tianjin Normal University, Tianjin, China, [4]Key Laboratory of Water Cycle and Related Land Surface Processes, Institute of Geographic Sciences and Natural Resources Research, Chinese Academy of Sciences, Beijing, China, [5]State Key Laboratory of Simulation and Regulation of Water Cycle in River Basin, China Institute of Water Resources and Hydropower Research, Beijing, China, [6]Department of Safety, Health, and Environmental Engineering, National Yunlin University of Science and Technology, Douliu, Taiwan, China, [7]Research Center for Soil and Water Resources and Natural Disaster Prevention, National Yunlin University of Science and Technology, Douliu, Taiwan, China, [8]Key Laboratory of Subsurface Hydrology and Ecological Effects in Arid Region, Chang'an University, Xi'an, China

Key Points:
- An innovative approach of identifying the unknown boundary conditions in groundwater basins is proposed
- Boundary conditions are captured by identifying anomalously high/low-permeability areas in a larger domain than a groundwater basin shape
- Hydraulic tomography facilitates the accurate identification of boundary conditions in groundwater basins

Correspondence to:
T.-C. J. Yeh,
yeh@hwr.arizona.edu

Citation:
Liu, F., Yeh, T.-C. J., Wang, Y.-L., Song, X., Lei, X., Wen, J.-C., et al. (2020). Potential of hydraulic tomography in identifying boundary conditions of groundwater basins. *Water Resources Research*, *56*, e2020WR028331. https://doi.org/10.1029/2020WR028331

Received 8 JUL 2020
Accepted 8 NOV 2020
Accepted article online 16 NOV 2020

Abstract This study investigates the potential of hydraulic tomography (HT) in identifying the boundary conditions of groundwater basins using numerical experiments. The experiment mimics the scenario of groundwater exploitation reduction in a pilot area of groundwater overexploitation control in the North China Plain. In this study, we propose an approach that integrates the HT concept and readily available groundwater monitoring data to identify the constant head and impermeable boundaries by mapping anomalously high- and low-permeability zones from HT surveys in a large-scale domain that encompasses the true groundwater basin. The resulting boundaries and conditions were then used in inversion of steady-state and transient-state simultaneous pumping tests and HT surveys of heterogeneity within the groundwater basin. The inversion results demonstrated significant advantages of HT surveys over multiple simultaneous pumping tests to identify boundary conditions and heterogeneity in the groundwater basin. Moreover, steady HT inversion outperforms transient HT inversion in capturing the true boundary conditions, leading to the better T estimates from steady HT inversion than those from transient HT inversion. Additionally, the study shows that accurate geological zonation information can significantly improve HT parameter estimations.

1. Introduction

Accurate simulations are crucial for basin-scale groundwater sustainable management (e.g., Cao et al., 2013; F. Liu et al., 2018; Yeh, 1992), and they require comprehensive knowledge of aquifer heterogeneity, boundary condition, and initial condition (H.-J. Liu et al., 2009).

Inverse modeling or model calibration has been a widely used means to acquire these pieces of information. Nevertheless, inverse modeling is to solve an ill-defined problem due to a lack of necessary information (Mao et al., 2013; Yeh et al., 2015). For example, unknown boundary conditions could lead to non-unique estimated parameters and the flow fields (Irsa & Zhang, 2012). As such, accurate inverse modeling has long been a challenge in studying groundwater processes (Carrera & Neuman, 1986; Dafflon et al., 2011; F. Liu et al., 2020).

More recently, Yeh and Liu (2000), Zhu and Yeh (2005), Xiang et al. (2009), and others have developed a new generation of inverse modeling approaches (hydraulic tomography, HT). Over past decades, it has been tested, validated, and demonstrated in synthetic experiments (e.g., Cardiff et al., 2009; Mohammadi & Illman, 2019; Y.-L. Wang et al., 2019), laboratory sandboxes (e.g., Illman et al., 2007; Luo et al., 2017; Z. Zhao et al., 2016), and field-scale aquifers (e.g., Berg & Illman, 2011; Bohling et al., 2007; Cardiff et al., 2020; Straface et al., 2007; Zha et al., 2016, and many others). Ultimately, HT has evolved as a mature technology for high-resolution aquifer characterization.

Relative to conventional aquifer tests or inverse modeling efforts using a single excitation, the superiority of HT stems from the fact that it yields a more detailed characterization of subsurface heterogeneity.

Conventional aquifer tests for characterizing large-scale aquifers are time-consuming and costly tasks, given the fact that it can only yield spatially averaged hydraulic parameters in a localized portion of a large aquifer. On the other hand, HT survey is analogous to computerized axial tomography (CAT) scan technology. It sequentially stresses the subsurface using pumping or injection tests at different locations to create multiple aquifer responses. During each stress, a large number of aquifer responses are collected in a well field. The responses collected during each stress at a different location are tantamount to a snapshot of aquifer heterogeneity from a different angle and perspective. In other words, each snapshot carries non-fully redundant information (Wen et al., 2020) and leads to an estimate of the spatial distribution of aquifer properties, and it is then cross validated and updated with a new snapshot. Consequently, synthesizing the multiple sets of aquifer signals to characterize spatial patterns of hydraulic parameters in the subsurface results in higher accuracy than conventional aquifer tests.

Most past HT inverse modeling studies used synthetic aquifers or sandboxes, in which boundary conditions are entirely known, and avoided the effects of uncertainty of boundary conditions. On the other hand, past inverse modeling of field aquifers generally enlarged the simulation domain (i.e., many times the correlation scales of hydraulic properties; Dagan, 2012) and assumed that the effects of boundaries were minimum. For example, Illman et al. (2009) and Zha et al. (2016) used a more extensive model domain than the well field's actual area to avoid suspicious boundary effects in the HT inversion. They delineated the locations and irregular shapes of the fault zone and the fracture zones. Such an approach has been widely recommended to estimate aquifer parameters in groundwater modeling for many years (H.-J. Liu et al., 2009).

Very few papers have investigated the effects of the unknown boundaries on the HT inversion. For instance, Sun et al. (2013) examined the influence of incorrect boundaries in parameter estimations. They reported that HT analysis with a misrepresentation of an impermeable boundary as a constant head boundary led to an estimate of a low-permeability zone near the constant head boundary. Using an approach different from the conventional inverse modeling approach, Jiao and Zhang (2014) proposed a two-dimensional inverse method to simultaneously estimate multiple hydraulic conductivities without specification of conditions at known aquifers' boundary locations, for both confined and unconfined aquifers under non-pumping or pumping conditions. Likewise, a similar method for three-dimensional steady-state aquifer inversion was developed by Zhang et al. (2014) to estimate aquifer hydraulic conductivities without exploiting HT's power.

Recently, Daranond et al. (2020) confirmed that HT could identify the impermeable boundaries as lower T zones in the vicinity of a 2-D synthetic buried-valley aquifer boundary, but the issue of constant head boundary identification was not investigated. Therefore, a comprehensive study of identifying the unknown boundary conditions (i.e., constant head boundary and impermeable boundary) of groundwater basins and their effects on the estimated T and S field is needed.

For these reasons, the objectives of this paper are to (1) demonstrate the advantages of HT survey over the multiple simultaneous pumping tests in identifying the unknown boundary conditions of groundwater basins under steady-state and transient-state scenarios and (2) investigate the effect of geological data on the performance of inverse models using the guessed boundary conditions. We hope that this study's results may inspire more studies on the integration of geological, other data, and HT concept in parameter estimation and identifying unknown boundary conditions of groundwater basins.

2. Methods

2.1. Groundwater Flow Model

This study assumes that the following partial differential equation can describe the two-dimensional, depth-averaged groundwater flow in heterogeneous confined aquifers:

$$\nabla \cdot [T(\boldsymbol{x}) \nabla H] + Q(\boldsymbol{x}_p) = S(\boldsymbol{x}) \frac{\partial H}{\partial t} \tag{1}$$

subject to the boundary and initial conditions:

$$H\Big|_{\Gamma_1} = H_1,\ [-T(\mathbf{x})\nabla H]\cdot\mathbf{n}\Big|_{\Gamma_2} = q,\ \text{and}\ H\Big|_{t=0} = H_0 \tag{2}$$

where, in Equation 1, H represents the total head (L), $\mathbf{x}$ is the position vector ($\mathbf{x} = (x, y)$, [L]), Q ($\mathbf{x}_p$) is the pumping rate per unit area (L/T) at the location $\mathbf{x}_p$, $T(\mathbf{x})$ is the transmissivity (L^2/T), and $S(\mathbf{x})$ is the storativity (–). Additionally, the right-hand term of Equation 1 becomes 0 when it describes steady-state groundwater flow. In Equation 2, H_1 is the specified head at boundary Γ_1, q is the prescribed flux at boundary Γ_2, $\mathbf{n}$ is a unit vector normal to Γ_2, and H_0 represents the initial head before stressing the aquifer.

In this study, solutions to Equations 1 and 2 are implemented in the VSAFT2 (Variably Saturated Flow and Transport 2-D) software developed by Yeh et al. (1993) available online (at http://tian.hwr.arizona.edu/downloads). The head solutions in time and space over the solution domain are then selected to estimate the fields of aquifer parameters (T and S) by an inverse algorithm described below.

2.2. Boundary Conditions Identification Approach

Mathematically, both the forward and inverse modeling of a steady-state flow are boundary value problems, albeit they require different boundary information to derive solutions. Forward modeling needs prescribed heads (the Dirichlet boundary) or fluxes (the Neumann boundary) and T values to solve the unique total head distribution. On the other hand, inverse modeling demands the fluxes around all boundaries and heads everywhere to derive unique T distributions. Notice that the T values and head gradients' requirements along the boundaries could replace the flux information (Yeh et al., 2015).

In the case of the forward modeling of transient flow, the knowledge of both T and S fields and initial conditions is a prerequisite, in addition to the boundary conditions as in the steady-state flow problems. Similarly, using transient flow data to identify T and S, one must have prescribed head distributions at different times and the boundary flux conditions.

In real-world aquifers, locations of sinks or sources, such as rivers and lakes, are often modeled by constant head boundaries in mathematical models, while faults, groundwater divides, and bedrock around the aquifers are conceptualized as the impermeable (no flux) boundaries.

Under steady flow situations, a large flux boundary can be thought of as the effects of a high-permeability zone near a constant head boundary, and a low flux boundary is due to the presence of a low-permeability zone.

For the transient behavior of heads at observation wells during a pumping test, the head change rate reduces and stabilizes once the drawdown reaches a source (or a constant head) boundary. Such behaviors could be interpreted as the effects of a zone with large T or S or high T/S values near the boundary. Meanwhile, a continuous increase in drawdown, as the drawdown encounters an impermeable boundary, may be interpreted as the effects of a low T or S or low T/S zone near the boundary.

The discussion above leads to the following hypothesis. If the groundwater basin boundary conditions are unknown, one can design a larger domain than the groundwater basin's actual size, and a constant head boundary surrounds the domain. Then, one can use the HT survey to map the high and low T and S regions, facilitating the definition of the groundwater basin's constant head or impermeable boundaries. Once the boundary conditions are identified, HT can yield detailed T or T/S fields.

2.3. Inverse Modeling Approach

We tested the above hypothesis using the Simultaneous Successive Linear Estimator (SimSLE) algorithm developed by Xiang et al. (2009). The SimSLE algorithm was modified from the Sequential Successive Linear Estimator (SSLE) (Zhu & Yeh, 2005). Unlike the SSLE method that sequentially assimilates the head data from discrete sources into the inversion process, the SimSLE algorithm simultaneously incorporates all the available aquifer responses to multiple pumping tests during HT surveys in the estimation of aquifer properties. This approach avoids the effects associated with the order of test on the estimates and thus improves computational efficiency. A brief description of the SimSLE algorithm is given below.

SimSLE assumes that the natural logarithms of T ($\ln T$) and S ($\ln S$) are random variables, and they are described by a given spatial statistics of the parameter fields (mean, variance, and correlation scale). The SimSLE then starts with a stochastic linear estimator (Priestley, 1981) to estimate the conditional effective values of the perturbations of $\ln T$ and $\ln S$, based on the observed head data.

Then, a successive linear estimator (SLE) is used to iteratively update the estimated T and S fields by assimilating the head data. Assuming f is an $N \times 1$ vector containing T or S estimates. The successive iteration procedure takes the following form:

$$f^{(r+1)} = f^{(r)} + \omega^{(r)T}\left(h - h^{(r)}\right) \tag{3}$$

where $f^{(r)}$ is the conditional expectation of f at iteration r ($r > 1$), h is an $m \times 1$ vector of the observed head, and $h^{(r)}$ is the simulated head at a given location and time obtained from the forward model using the estimated parameters at iteration r. The superscript T represents the transpose. When $r = 0$, the estimate starts from T and S's initial guess fields (uniform mean or zonal mean, in this study). Afterward, the conditional mean estimates are successively improved by the weighted differences between the observed and the simulated values. The weighting coefficient matrix ω ($m \times N$) is updated by the following equation:

$$[\varepsilon_{hh} + Q_d + \theta diag(\varepsilon_{hh})]\omega = \varepsilon_{hf} \tag{4}$$

where ε_{hh} is the conditional auto-covariance matrix ($m \times m$) of observation data and ε_{hf} is the conditional cross-covariance matrix ($m \times N$) between observed head data and parameter f. In Equation 4, θ is a stability multiplier and $diag(\varepsilon_{hh})$ is a stability matrix, which is the diagonal elements of the ε_{hh} matrix. SimSLE stabilizes the solution by adding a dynamic stabilizer to the diagonal elements of the ε_{hh} matrix (Pujol, 2007). Q_d is a diagonal matrix of variances of measurement errors. The estimates of covariance matrix ε_{hh} and cross-covariance matrix ε_{hf} are calculated by the first-order numerical approximation (Yeh & Liu, 2000):

$$\varepsilon_{hh}^{(r)} = J_{hf}^{(r)} \varepsilon_{ff}^{(r)} J_{hf}^{(r)T}, \quad \varepsilon_{hf}^{(r)} = J_{hf}^{(r)} \varepsilon_{ff}^{(r)} \tag{5}$$

where $J_{hf}^{(r)}$ ($m \times N$) is the sensitivity matrix for the observed head data with respect to the change of estimated parameter f at iteration r. The sensitivity matrix is calculated by the adjoint state method (Xiang et al., 2009).

The residual covariance function reflects the improvements in the parameter estimates and reduction in the estimated parameter uncertainty by successive iterations (Zha et al., 2014). The covariance matrix ε_{ff} ($N \times N$) is unconditional and is essentially the auto-covariance matrix of parameter f at $r = 0$. The exponential model is used for the covariance function in this study. For $r > 0$, the covariance matrices become conditional or residual covariance, and are updated according to the following equation:

$$\varepsilon_{ff}^{(r+1)} = \varepsilon_{ff}^{(r)} - \omega^{(r)T} \varepsilon_{hf}^{(r)} \tag{6}$$

The iterative procedure continues until one of the following two convergence criteria is met. That is, the change in variances between the current estimated hydraulic properties and prior iterations is smaller than a given tolerance, or the change of simulated heads between successive iterations is smaller than the user-specified head tolerance (Xiang et al., 2009). Mathematically, this updating procedure is similar to that in the Kalman filter algorithm (Schöniger et al., 2012) during the assimilation of new information.

For evaluating the estimates from SimSLE, we used the following performance metrics: the coefficient of determination (R^2), the mean square error (L_2), the slope, and the intercept of the regressed linear relationship between the estimates and the true parameters. Overall, a higher R^2 represents a better result, while a smaller L_2 value means the better estimates. The closer the slope of the linear regression line to 1 and the intercept to 0, the better the estimates are.

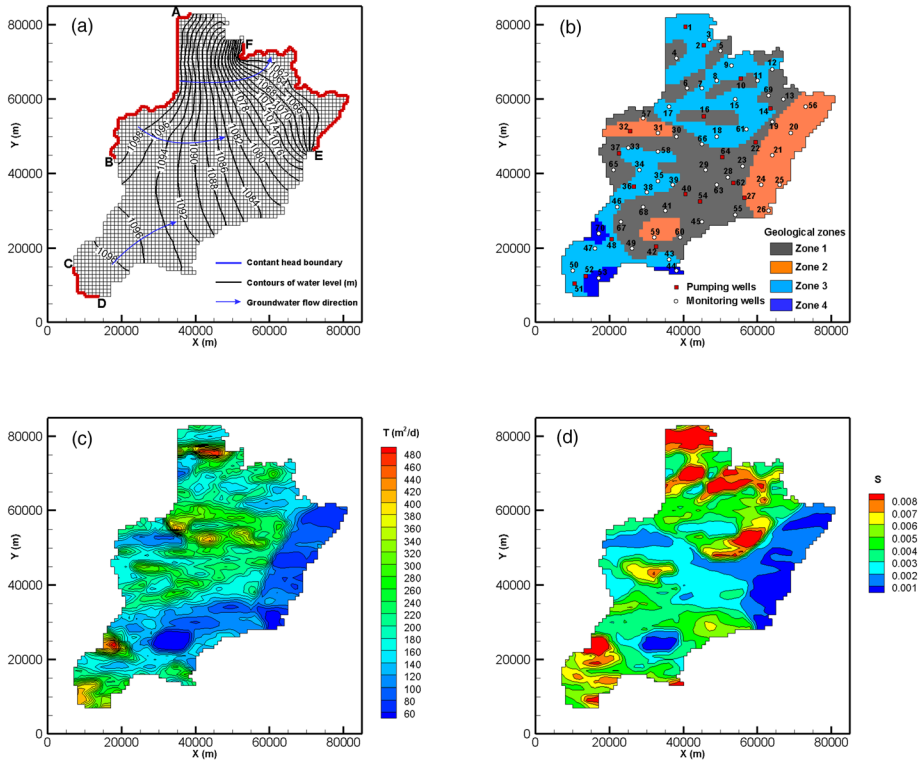

Figure 1. Grid discretization, true boundary condition, and steady-state flow field with no pumping (a), the layout of pumping and monitoring wells as well as geological zones (b), reference transmissivity (c), and storativity (d) fields of the synthetic groundwater basin.

3. Numerical Experiments

3.1. Forward Modeling of the Reference Groundwater Basin

The prototype of the synthetic groundwater basin is the Heilonggang (HLG) plain in the North China Plain (NCP), where the total amount of groundwater exploitation has considerably reduced due to agricultural water conservation projects and water transfer from the middle route of the South-to-North Water Diversion Project since 2014 (Y. Zhao et al., 2017). As a result, the groundwater rebound and changes in flow fields are anticipated. This response is an excellent opportunity to estimate the NCP's hydraulic heterogeneity by utilizing the aquifer signals with operational changes of existing wells as a basin-scale HT (F. Liu et al., 2020).

The aquifers in the NCP are an aquifer-aquitard system (Cao et al., 2013). The synthetic groundwater basin, therefore, was designed to mimic the confined aquifer in the HLG plain. The confined aquifer's T and S values vary from 10 to 480 m^2/day, and from 0.001 to 0.008, respectively (B. Wang, 2011). The confined groundwater mainly flows from west and southwest to northeast (Figure 1a).

The shape of the synthetic aquifer imitated the geometry of the groundwater basin. This basin was discretized into 2,720 rectangular elements and 2,896 nodes with element dimensions 1 km × 1 km (Figure 1a). The true boundary conditions were assumed to be as follows. The constant head boundary was assigned to the A-B, C-D, and E-F segments with head values of 1,100, 1,100, and 1,060 m. The remaining boundary segments perpendicular to the groundwater level contours were prescribed as the impermeable boundaries (Figure 1a). Seventy wells (18 pumping wells and 52 monitoring wells) were considered, and the well layout was similar to those in the actual groundwater basin (Figure 1b).

According to geological data (Wei, 2018), we divided the aquifer into four geological zones (Figure 1b). Each zone had different T values, namely, Zone 1 (120–240 m^2/day), Zone 2 (<120 m^2/day), Zone 3 (240–360 m^2/day), and Zone 4 (360–480 m^2/day). To represent the aquifer's multiscale heterogeneity, we

Table 1
Design of Pumping Tests in the Steady-State Simulation

	Stress	Pumping wells	Pumping rate per well (m^3/day)
Scenario A	Stress 1	18 pumping wells	−3,000
Scenario B	Stress 1	6 pumping wells (1/10/32/51/54/62)	−3,000
	Stress 2	6 pumping wells (2/22/27/36/48/52)	−3,000
	Stress 3	6 pumping wells (14/16/37/40/42/64)	−3,000

assigned the mean ln$T$ (m^2/day) values 5.1, 4.38, 5.4, and 5.68 to Zones 1, 2, 3, and 4, respectively. Likewise, the mean ln$S$ for each zone is −5.81, −6.91, −5.12, and −4.89, respectively. Further, the variances of ln$T$ and ln$S$ for each zone were 0.1, due to low heterogeneity in each zone. The correlation scales were 20 km in the east-west direction and 5 km in the north-south direction. Different random seeds were used to generate independent stochastic fields of reference T and S for each geological zone (Figures 1c and 1d) using a random field generator (Gutjahr, 1989) embedded in VSAFT2 software.

For steady-state flow models, two scenarios (Scenarios A and B) were considered (Table 1) to explore the effectiveness of simultaneous and sequential pumping events for identifying boundary conditions and aqui-

Table 2
Design of Pumping Tests in Transient-State Experiments

Scenario	Stress	Event	Pumping well ID	Pumping rate per well (m^3/day)	Time period (days)	Status
Scenario C	Stress 1	Event 1	1/10/32/51/54/62	−8,000	0 – 1,000	normal rate
				−4,000	1,001 – 2,000	reduction
				0	2,001 – 3,000	shut down
		Event 2	2/22/27/36/48/52	−8,000	0 – 1,000	normal rate
				0	1,001 – 2,000	shut down
				−4,000	2,001 – 3,000	reduction
		Event 3	14/16/37/40/42/64	0	0 – 1,000	shut down
				−8,000	1,001 – 2,000	normal rate
				−4,000	2,001 – 3,000	reduction
Scenario D	Stress 1	Event 1	1/10/32/51/54/62	−8,000	0 – 1,000	normal rate
				−4,000	1,001–2,000	reduction
				0	2,001 – 3,000	shut down
		Event 2	2/22/27/36/48/52	−8,000	0 – 1,000	normal rate
				0	1,001 – 2,000	shut down
				−4,000	2,001 – 3,000	reduction
		Event 3	14/16/37/40/42/64	0	0 – 1,000	shut down
				−8,000	1,001 – 2,000	normal rate
				−4,000	2,001–3,000	reduction
	Stress 2	Event 1	2/22/27/36/48/52	−8,000	0 – 1,000	normal rate
				−4,000	1,001 – 2,000	reduction
				0	2,001 – 3,000	shut down
		Event 2	14/16/37/40/42/64	−8,000	0 – 1,000	normal rate
				0	1,001 – 2,000	shut down
				−4,000	2,001 – 3,000	reduction
		Event 3	1/10/32/51/54/62	0	0 – 1,000	shut down
				−8,000	1,001 – 2,000	normal rate
				−4,000	2,001 – 3,000	reduction
	Stress 3	Event 1	14/16/37/40/42/64	−8,000	0 – 1,000	normal rate
				−4,000	1,001 – 2000	reduction
				0	2,001 – 3,000	shut down
		Event 2	1/10/32/51/54/62	−8,000	0 – 1,000	normal rate
				0	1,001 – 2,000	shut down
				−4,000	2,001 – 3,000	reduction
		Event 3	2/22/27/36/48/52	0	0 – 1,000	shut down
				−8,000	1,001 – 2,000	normal rate
				−4,000	2,001 – 3,000	reduction

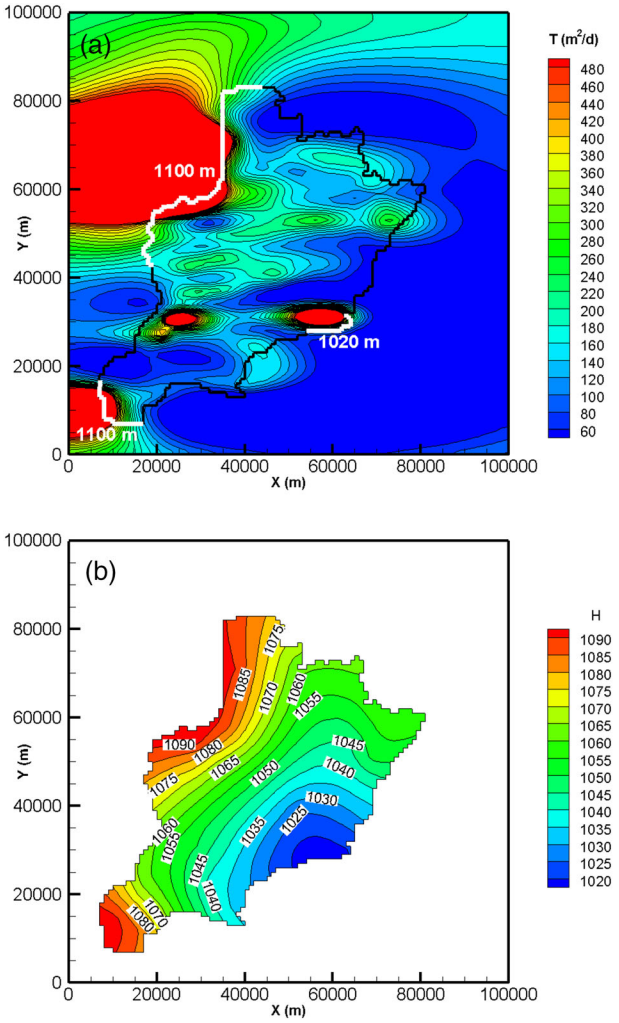

Figure 2. The inferred boundary conditions (white lines for constant head boundaries and black lines are impermeable boundaries) in the Scenario A (steady-state simultaneous pumping event), based on (a) the estimated *T* field using a square aquifer, and (b) the flow field obtained from the observed head data.

fer parameters. As shown in Table 1, Scenario A represents the situation where 18 wells (see Figure 1b) were discharging simultaneously at a rate of 3,000 m^3/day. Scenario B is a tomographic survey (or an alternating pumping situation) with three pumping stresses, and each stress involved pumping six different wells at a rate of 3,000 m^3/day. The well numbers are listed in parentheses in Table 1 and locations are indicated in Figure 1b.

Scenarios C and D were considered in transient-state flow experiments (Table 2). In Scenario C, one stress was imposed, which included three simultaneous pumping events. Each event occurred at a group of wells, over three periods (0–1,000, 1,001–2000, and 2001–3,000 days) with pumping/reduction/shutdown activities. In Scenario D, we designed the pumping operations to instigate a basin-scale HT survey. Three stresses were employed; each stress had three operational events and involved a different group of wells at different locations, operating at different pumping/reduction/shutdown patterns over the three periods.

The design of these events was to imitate municipal pumping systems in the HLG plain. Specifically, the first time frame (0–1,000 days) represents the effect of normal pumping operations before implementing the groundwater exploitation reduction program at the year of 2014. The second time frame (1,001–2,000 days) and the last time frame (2,001–3,000 days) signify the initial and late stage of regional groundwater-pumping reduction. The pumping rates were designed such that each pumping event stresses most of the aquifer, leading to the superposition between the stressed portions of different pumping events. Such operational variations of pumping wells led to continuous changes in the groundwater flow field and created a basin-scale HT survey.

During transient flow simulations, the aquifer's steady-state responses under no pumping events were used as initial conditions for calculating transient head variations induced by the groundwater exploitation reduction. Simulated groundwater responses for these scenarios were then sampled for the inverse modeling efforts.

3.2. Inverse Model Experiments

The inverse simulation in this study consisted of two steps: (1) identification of boundary conditions of the groundwater basin using a square domain much larger than the groundwater basin, which was circumscribed by constant head boundaries at four sides, and (2) estimation of the parameters using the boundary conditions obtained in (1).

For the first step, we chose a square domain (100 km × 100 km) larger than the reference groundwater basin and discretized it with the same size elements as those for the reference groundwater basin. We then assigned the maximum observed head (1,100 m) in the groundwater basin as the constant head boundary values for the square domain's four sides. For initial conditions in transient simulations, a steady-state flow field without groundwater pumping was used as the initial head field within the groundwater basin, while domain outside the basin was assumed to be the constant head value (1,100 m) everywhere. The initial *T* and *S* fields for the inverse model of the square domain were assumed to be homogeneous, using *T* and *S*'s mean values for Zone 1.

The inversion results from the square aquifer were intended to indicate the possible types and head values of boundary conditions only. These guessed boundary conditions were then assigned to the groundwater basin for the inverse models, and the performance of parameter inversions was examined.

After the boundary conditions were estimated, we investigated the effects of prior information on the estimated parameters based on two cases. In Case 1, the prior *T* and *S* fields for the inverse model were

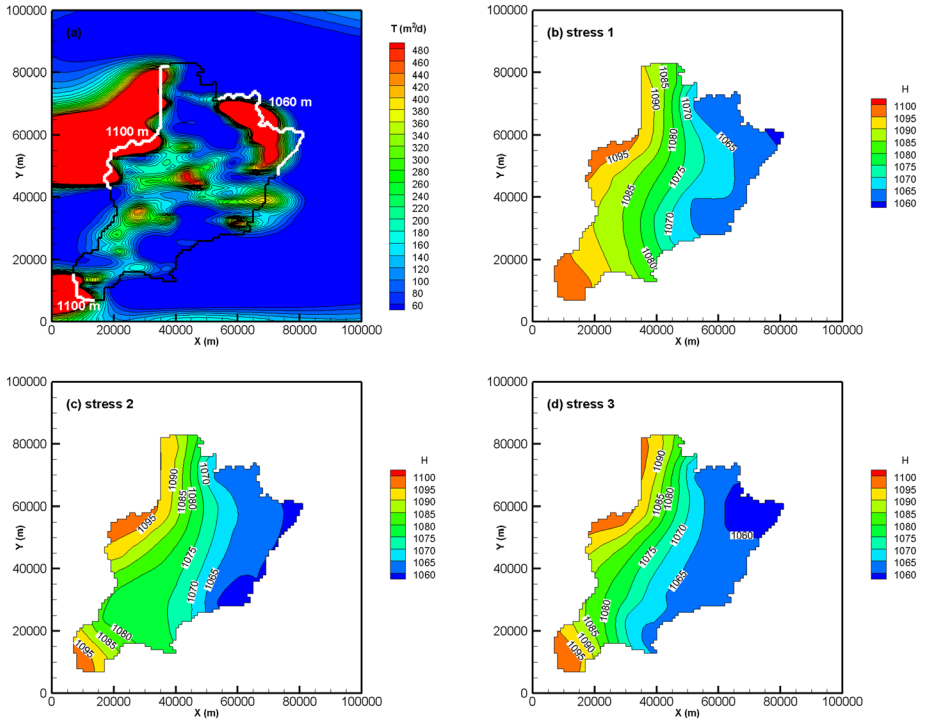

Figure 3. The inferred boundary conditions (white lines for the constant head boundaries and black lines are the impermeable boundaries) in the Scenario B (steady-state HT), based on (a) the estimated *T* field using a square domain, and (b-d) the flow fields obtained from the observed head data.

homogeneous, with their values equal to those of Zone 1 in the reference basin properties due to their prevalence in the basin (Figure 1b).

As the importance of incorporating accurate geological data in HT surveys has been emphasized for sandbox experiments and a highly heterogeneous field site (Z. Zhao et al., 2016; Z. Zhao & Illman, 2018), we assumed, in Case 2, that the spatial patterns of the geological zones over the groundwater domain were known exactly (Figure 1b) via available borehole logs, geological maps, and cross sections. That is, each zone's prior *T* and *S* values were set to the *T* and *S* mean values of the corresponding zone in the reference fields.

4. Results and Discussion

4.1. Identification of Unknown Boundary Conditions

4.1.1. Steady-State Simulation

The estimated *T* field over the entire square aquifer, based on simultaneous pumping tests at 18 wells (Scenario A), is shown in Figure 2a. Noticeably, the exceptionally high-permeability (red) zones appear near the northwest and southwest constant head boundaries of the reference groundwater basin (indicated by the white lines). However, a small high *T* zone emerges near the true impermeability boundary in the lower eastern part of the reference basin. Similarly, low-permeability zones are incorrectly identified near the true constant head boundaries in the basin's northeastern corner. Nonetheless, the zones with exceptionally low permeable values coincide with most of the reference basin's impermeable boundaries.

Subsequently, we interpreted the simulated head data at the observation wells under this scenario by using kriging without specifying correlation scales, and the contoured head distribution is illustrated in Figure 2b. Generally, it indicates that the northwest and southwest boundary segments have high head values close to 1,100 m, and the southeastern segment points to a groundwater depression, with a low head value approaching 1,020 m. From these pieces of information, guessed boundary conditions for the inverse model in Scenario A were thus determined (Figure 2a).

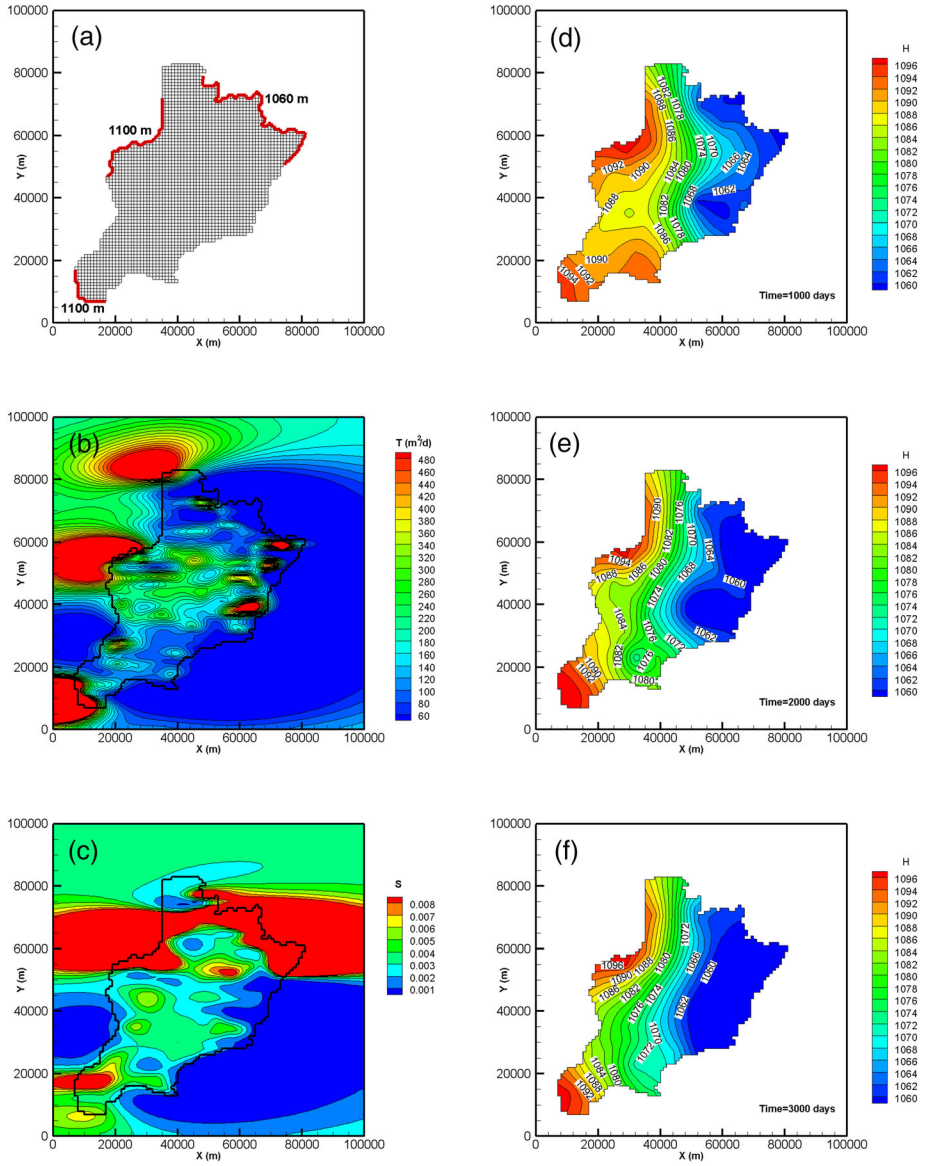

Figure 4. The inferred boundary conditions (red lines are the constant head boundaries and the rest is the impermeable boundaries) (a) for inverse models in the Scenario C (transient simultaneous pumping), based on the estimated *T* (b) and *S* (c) fields using a square domain, and the flow fields obtained from the observed head data at selected time 1000 (d), 2000 (e) and 3000 days (f).

In the case of using HT survey (Scenario B), the estimated *T* field over the entire square domain (Figure 3a) shows that the locations of exceptionally high and low *T* zones are closer to the true constant head and impermeable boundaries of the reference groundwater basin (Figure 1a) than Scenario A (Figure 2a). Such results manifest the viability of HT survey for identifying the boundary shape and the characteristics. Based on the results, the constant head boundary conditions were assigned to the segments near the red areas indicative of the exceptionally high *T* zones, while the remaining segments with low-permeability were assigned as impermeable boundaries.

The kriged head fields using head data at the observation wells during the three stresses of the HT are shown in Figures 3b–3d. The three steady-state head fields show a common general feature: Groundwater flows from west and southwest to northeast. Given that the contour of 1,095 m occurs inside the northwest and southwest boundary segments, the head values for both two segments were extrapolated to be 1,100 m

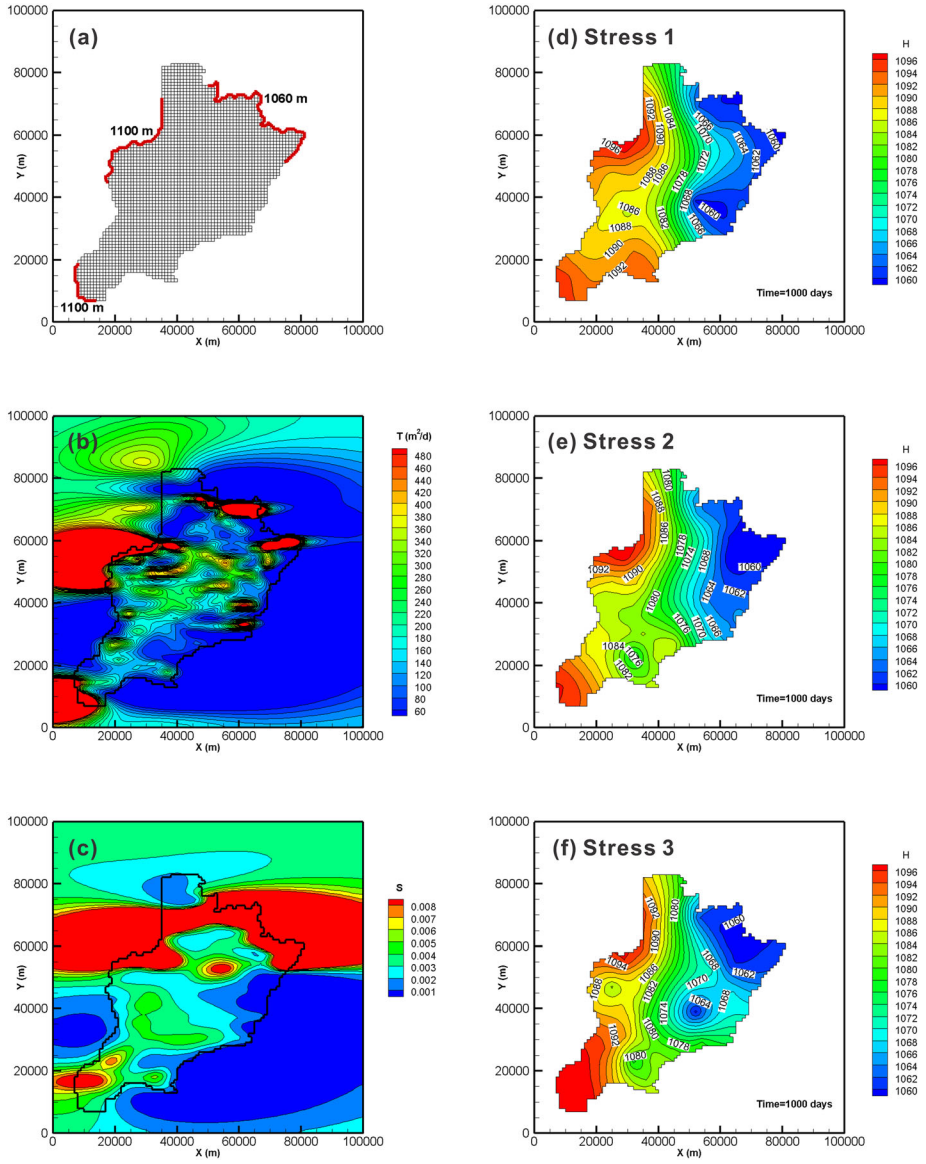

Figure 5. The inferred boundary conditions (red lines are the constant head boundaries and the rest is the impermeable boundaries) (a) for inverse models in the Scenario D (transient HT), based on the estimated *T* (b) and *S* (c) fields using a square aquifer, and the flow fields obtained from the observed head data at time 1000 days for stress 1 (d), stress 2 (e) and stress 3 (f).

(Figure 3a). Since heads throughout the line of the northeast boundary segments, where high *T* exists, range from 1,060 to 1,065 m (Figures 3b–3d), the head value of the northeast constant head boundary was assumed to be 1,060 m. Afterward, these guessed boundary conditions of Scenario B shown in Figure 3a were then applied to this scenario's inverse model.

Albeit a hydraulic head contour map could shed some light on the boundary (Freeze & Cherry, 1979; Walton, 1970; Yeh et al., 2015), it is likely subjective and uncertain, given the fact that the natural aquifer systems are complex, observation wells are sparse, and their sampling times are intermittent. In other words, a hydraulic head map in a real-world basin is likely highly uncertain. Even in our hypothetical groundwater basin, these steady-state head fields, interpolated and extrapolated from exact data from observation wells (Figures 2b and 3b–3d), only provide a general indication of groundwater highs and lows locations, in turn, the likely flow directions. Under this hypothetical case, the interpretation's accuracy would depend on the density of observation wells and the flow complexity. For example, the northeastern head boundary

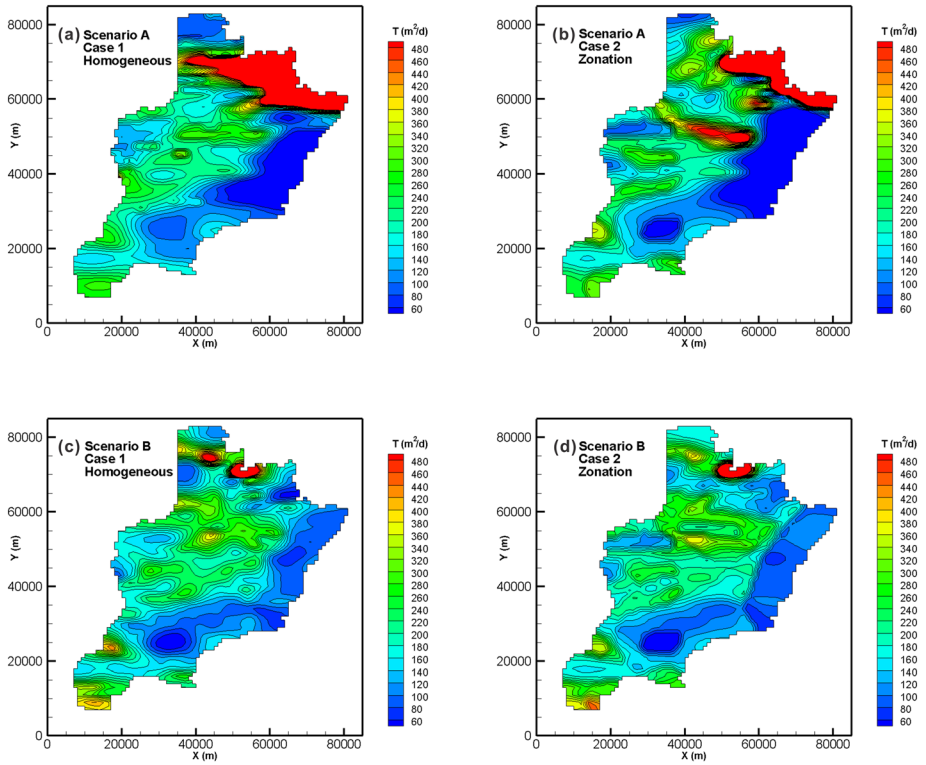

Figure 6. The estimated *T* fields from (a) Scenario A (steady-state simultaneous pumping), Case 1 (homogeneous prior); (b) Scenario A, Case 2 (zonal prior); (c) Scenario B (steady-state HT), Case 1; and (d) Scenario B, Case 2.

(E-F segment in Figure 1a) is not readily identifiable since the flow may detour to the southeastern segment (Figure 2b), which may be incorrectly perceived as a constant head boundary (Figure 2a). For these reasons, it is challenging to ascertain constant head and no-flow boundaries, the same as to estimate *T* based on head distributions and intuition alone. On the other hand, the inverse modeling effort, which simultaneously considers aquifer permeability, water level, pumping information, and the governing flow equation, is deemed appropriate and rational. Furthermore, HT cross-validates and adjusts the estimated locations to reduce the uncertainty in boundary condition locations.

4.1.2. Transient-State Simulation

Our proposed approach for identifying the boundary condition rests upon the significant change in hydraulic properties near the reference groundwater basin's actual boundaries. Besides, the inversion of the steady-state problem requires less information than the transient problem. We thus postulated that the steady-state HT approach might deliver better estimates of the boundaries. On the other hand, steady-state conditions might not exist in all real-life situations. For these reasons, we also identified unknown boundary locations and conditions, using the transient flow data from the simultaneous and HT tests, for Scenarios C and D, respectively.

Scenario C utilized the transient data induced by the simultaneous pumping tests, while Scenario D used the transient HT survey to estimate *T* and *S* fields from the square domain for deducing the boundary conditions of the groundwater basin. Figures 4b and 4c are the estimated *T* and *S* fields in Scenario C, and Figures 5b and 5c are those estimates in Scenario D. Overall, the estimated boundary conditions using HT (Scenario D, Figure 5a) are slightly closer to the true ones than those from the simultaneous pumping event (Scenario C, Figure 4a). Again, the results further substantiate the robustness of HT.

If we compare Figure 3a and Figure 5a, as expected, we find that the estimated boundary conditions from steady-state HT are slightly superior to those from the transient HT, in particular at the northwest and northeast corners of the reference basin.

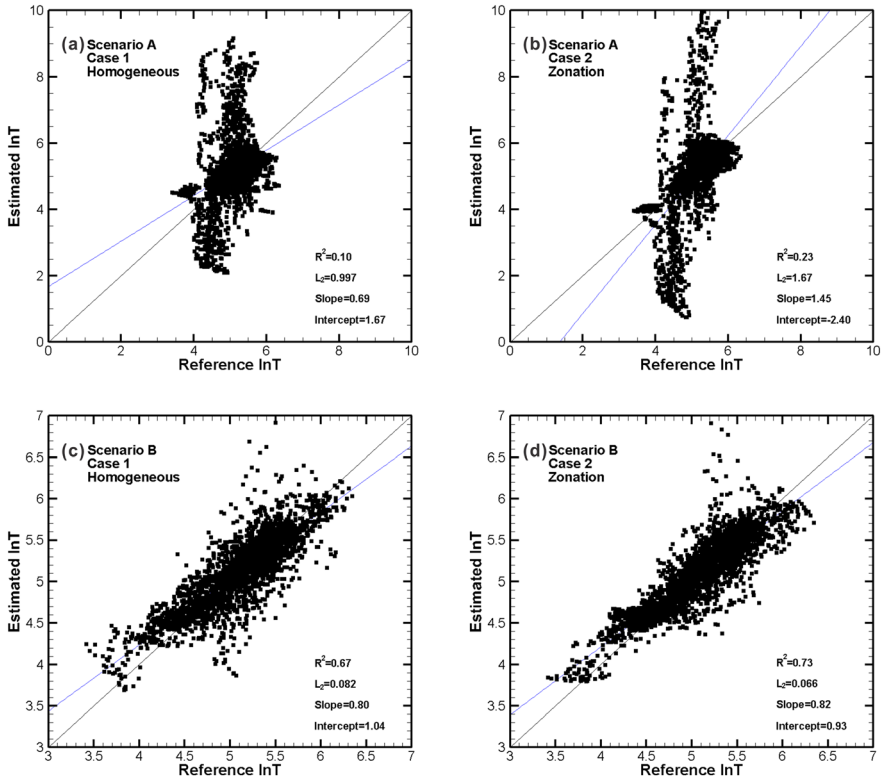

Figure 7. Scatterplots of reference versus estimated values of the transmissivity for (a) Scenario A (steady-state simultaneous pumping event), Case 1 (homogeneous prior); (b) Scenario A, Case 2 (zonal prior); (c) Scenario B (steady-state HT), Case 1; and (d) Scenario B, Case 2.

These results suggest that the boundary segments within the anomalously high *T* and *S* zones (i.e., red areas in Figures 4b and 4c) should be treated as constant head boundaries (i.e., red lines in Figure 4a). The segments bounded by low-permeability zones (i.e., blue areas in Figures 4b and 4c) should be conceptualized as impermeable boundaries.

Next, we determined the boundary head values. Given that the flow fields are time-variant in Scenario C with only one stress, the observed head data at selected time 1,000, 2,000, and 3,000 days were interpolated and extrapolated to obtain the three fields of head distribution (Figures 4d–4f). By synthesizing the contours of water levels at selected times, the guessed head values for constant head boundaries at the northwest and southwest were set to be 1,100 m, and the head value for the northeast boundary was assumed to be 1,060 m (Figure 4a).

As regards to Scenario D (HT survey), the boundary segments in the red areas (i.e., anomalously high *T* and *S* zones), were assigned as constant head boundaries (Figures 5b and 5c). On the other hand, those segments distributed in the blue areas (i.e., abnormally low *T* and *S* zones) were treated as impermeable boundaries (Figures 5b and 5c). Notice that these assigned boundaries (red lines in Figure 5a) are slightly different from those in Figure 4a, particularly at the left-hand side of the northeast boundary.

We then used observed head data at 1,000 days in each stress to yield the spatial patterns of head contours by the kriging method (Figures 5d–5f). These flow fields show different head distributions, but they all indicate that groundwater flows from the western and southwestern boundaries to northeast boundaries. The head values of the western and southwestern boundary segments were then extrapolated to be 1,100 m, while the value for the northeastern head boundary was 1,060 m (Figure 5a).

4.2. Estimates Using the Identified Boundary Conditions

4.2.1. Scenarios A and B (Steady Flows)

The estimated ln*T* field for the two cases (i.e., uniform and zonal priors) in Scenarios A and B, and their associated scatterplots and performance metrics from steady-state inversions are presented in Figures 6 and 7.

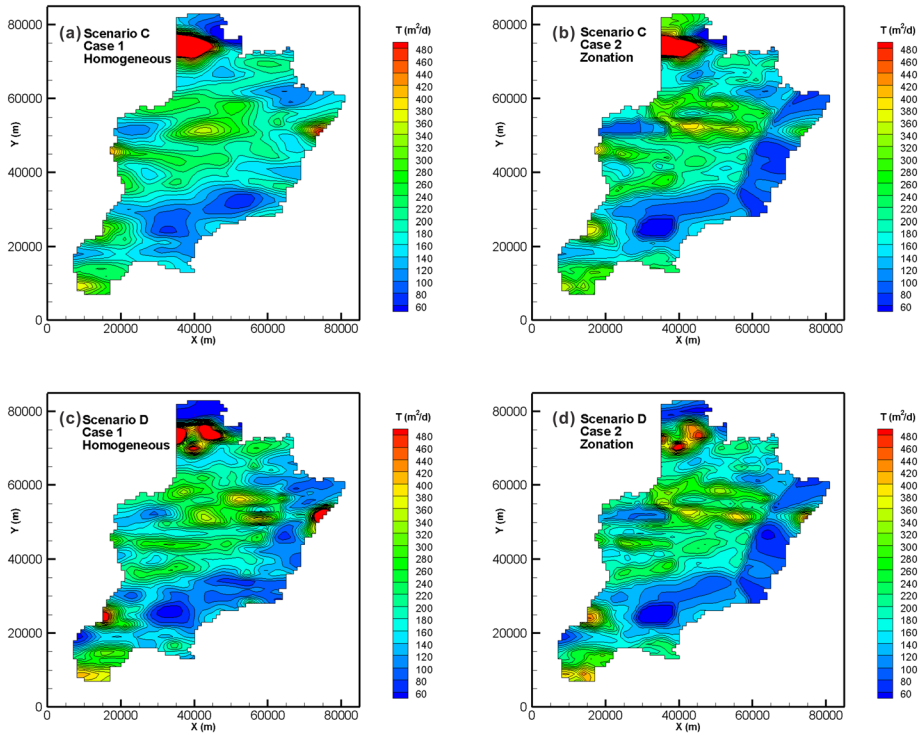

Figure 8. The estimated T fields from (a) Scenario C (transient simultaneous pumping event), Case 1 (homogeneous prior); (b) Scenario C, Case 2 (zonal prior); (c) Scenario D (transient HT), Case 1; and (d) Scenario D, Case 2.

For the simultaneous pumping tests (Scenario A), both cases (Figures 6a and 6b) show large red (exceptionally high T) zones at the incorrectly assigned impermeable boundary (black lines in the northeast of the basin, Figure 2a), but Case 2 (Figure 6b) shows a narrower red zone due to the effect of the prior zonal information. Examining Figures 6a and 6b, we observe that the estimated T field within the basin of Case 1 (uniform prior) is much smoother than that from Case 2 (zonal prior). More importantly, the main features of high T and low T zones from Case 1 are missing, indicating the loss of some essential information on aquifer heterogeneity. The associated scatterplots of estimated versus true ln$T$ and their performance statistics for these two cases are displayed in Figures 7a and 7b. From these figures, we observe that the incorrect northeast impermeable boundaries led to poor estimates of T within the groundwater basin despite the uniform or zonal prior information.

In Scenario B where HT was used to identify the boundaries, as we mentioned previously, the estimated boundary conditions are close to those of the true boundary conditions. Figures 6c and 6d show that no anomalously high T (red) estimates near the northeast corner of the basin, compared with Figures 6a and 6b, despite if the uniform (Case 1) or zonal (Case 2) priors were used. The scatter plots and performance metrics for these two cases are illustrated in Figures 7c and 7d. Notice the axis scales in Figures 7c and 7d are smaller than those in Figures 7a and 7b. From these figures, we observe that the estimates in both cases in Scenario B are superior to the two cases in Scenario A, where a large portion of the boundaries was incorrectly identified. These scatter plots also demonstrate that the use of zonal prior information leads to better estimates than uniform prior information.

In summary, the estimated T field from a steady-state HT survey (Scenario B) is more accurate than that from simultaneous pumping tests (Scenario A), suggesting that the HT survey identifies much more accurate boundary conditions than multiple simultaneous pumping tests. Additionally, the use of accurate geological data as the prior information can improve parameter estimations' performance, compared with uniform prior information. On the other hand, Z. Zhao et al. (2016) demonstrated that an inaccurate geological zonation model could have deleterious impacts on parameter estimations.

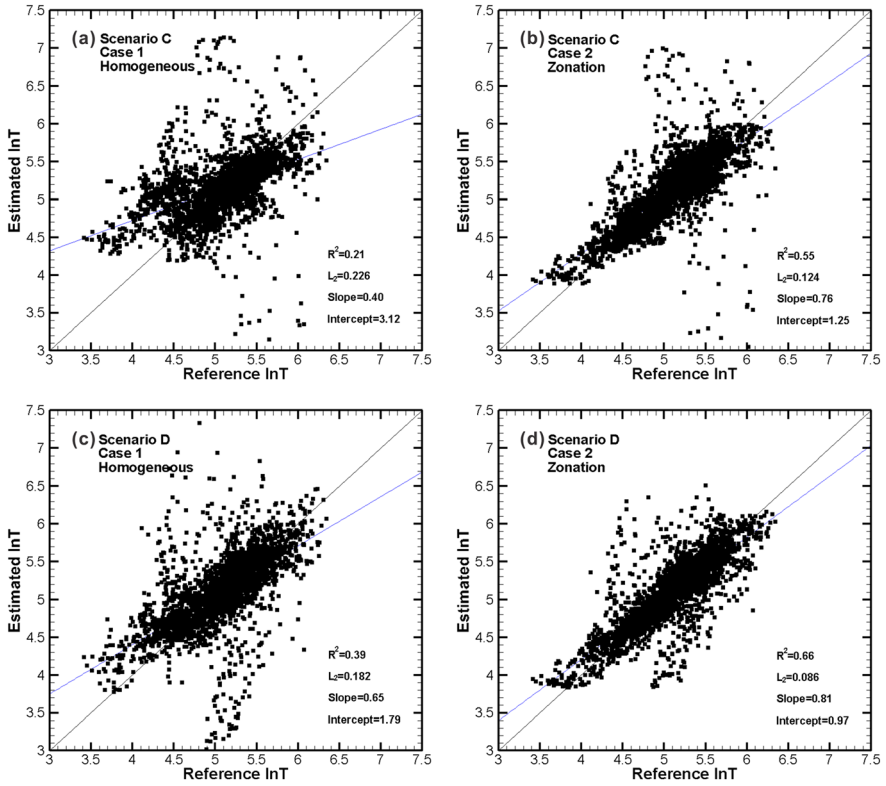

Figure 9. Scatterplots of reference versus estimated values of the transmissivity for (a) Scenario C (transient simultaneous pumping event), Case 1 (homogeneous prior); (b) Scenario C, Case 2 (zonal prior); (c) Scenario D (transient HT), Case 1; and (d) Scenario D, Case 2.

4.2.2. Scenarios C and D (Transient Flows)

The estimated *T* fields from Case 1 (uniform prior) and Case 2 (zonal prior) in Scenario C (simultaneous pumping tests), using the guessed boundary conditions and transient-state data, are exhibited in Figures 8a and 8b. The corresponding estimates from Cases 1 and 2 in Scenario D (HT survey) are depicted in Figures 8c and 8d. Recall that these two scenarios' boundary conditions generally agree with those in the reference groundwater basin with slight differences in the northeast corners between Scenarios C and D (Figures 4a and 5a). A visual examination of Figure 8 reveals that these estimated *T* fields are similar but different in the details. As shown in their scatter plots and performance metrics in Figure 9, we see that the result of Case 2 in Scenario D is superior to other cases and scenarios. Also, we notice that the estimates from Case 2 in Scenario C (Figure 9b) are better than those from Case 1 in Scenario D (Figure 9c). As indicated by this finding, under seemly correct boundary conditions, zonation as the prior information has a more profound impact than those of HT with uniform prior information. On the other hand, HT using the zonation's prior information yields a better characterization of the groundwater basin than the simultaneous pumping tests using the same prior information (Figures 9b and 9d).

Estimates of *S* field for the two cases in Scenarios C and D are displayed in Figure 10. Again, overall, these estimates are similar to those of the reference field of the groundwater basin (Figure 1d). The scatter plots and performance metrics are exhibited in Figure 11. Similar to the results of *T* estimates, Case 2 in Scenario D outperforms the rest. Likewise, the estimated *S* field in the simultaneous pumping tests using zone prior information is slightly better than in Case 1 of Scenario D (HT with uniform prior information of *S*). Consistent with *T* estimates results, the *S* estimates using HT with prior information of *S* zones are closer to the reference field than those based on the simultaneous pumping tests with the same prior zone information (Figures 11b and 11d).

We find anomalous outlines in the scatter plots (Figure 11) to be the *S* estimates in the vicinity of the northern boundary (i.e., the northernmost red areas in Figure 10). They may be ascribed to inaccurate

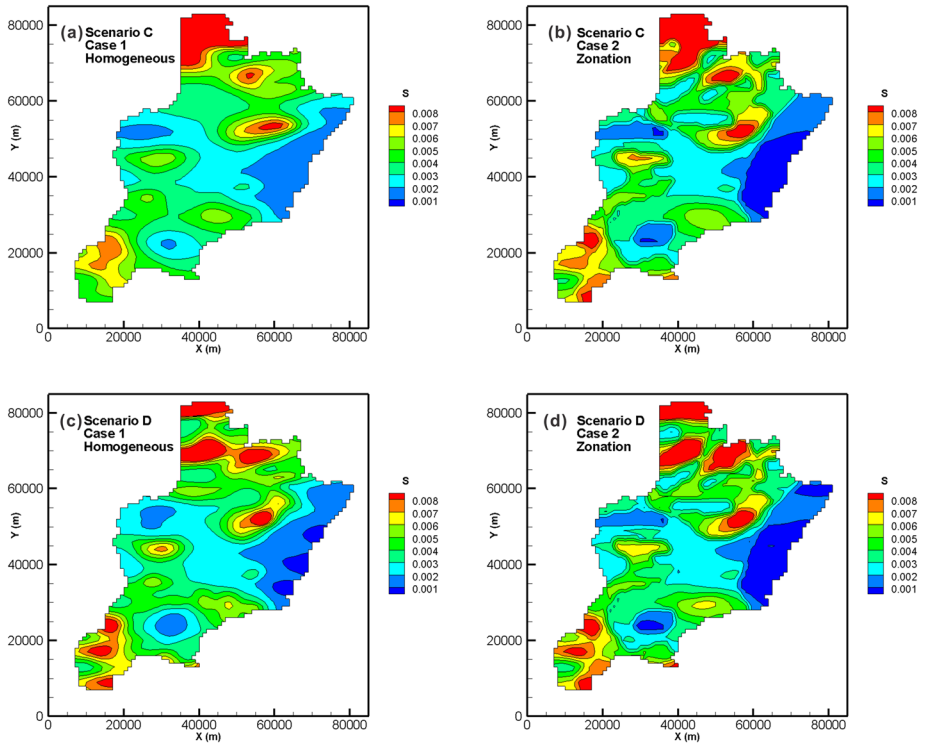

Figure 10. The estimated *S* fields from (a) Scenario C (transient simultaneous pumping event), Case 1 (homogeneous prior); (b) Scenario C, Case 2 (zonal prior); (c) Scenario D (transient HT), Case 1; and (d) Scenario D, Case 2.

identification of northern boundary conditions. In other words, a small section of the northern boundary that should have been a constant head boundary was wrongly assigned as an impermeable boundary, which led to the anomaly in *S* estimates.

These outliers occurred at Zone 3 of the geological zonation (Figure 1b), and they are worse in Case 2 (prior zonation) than in Case 1 (uniform prior) of the two scenarios. This deterioration is owing to differences in initial guess values of ln*S* between Case 1 and Case 2. The initial ln*S* value for Zone 3 in Case 2 is −5.12 (the mean reference ln*S* values in this area) and is larger than the initial ln*S* value (−5.81) for the entire basin in Case 1, which is based on the mean value of the Zone 1 because of its dominance over the entire basin (see section 3.2). Thus, such a difference in initial guess values of ln*S* exacerbates the effects of inaccurate boundary conditions in the north part of the basin. That is, the large the mean value is, the large the perturbation is. Despite these outliers, *S* estimates in other parts of the basin are significantly improved by incorporating accurate geological zones as prior information and using HT.

Lastly, a comparison of *T* estimates in Cases 1 and 2 of Scenario B (Figures 7c and 7d) and those in Cases 1 and 2 of Scenario D (Figures 9c and 9d) manifests that using steady-state HT head data with either uniform or zonal prior information could lead to more robust *T* estimates than transient HT data. Such results stem from the fact that transient data may carry a rich history of spatial heterogeneity encountered during flow events, but they are an accumulative effect of *T* and *S*, boundary fluxes, and initial conditions (more than twice the number of unknowns than in steady-state cases). These factors' complex interactions make deciphering them from the transient data difficult unless complete necessary information is available (see section 2.2).

Overall, the transient HT survey (Scenario D) captures more accurate information on boundary conditions than multiple simultaneous pumping tests (Scenario C). As a result, the estimated *T* and *S* fields from the transient HT survey are closer to the true fields than their conventional pumping test counterparts. Moreover, using an accurate geological zonation as initial guesses for inverse models can improve the parameter estimations and characterize aquifer heterogeneity.

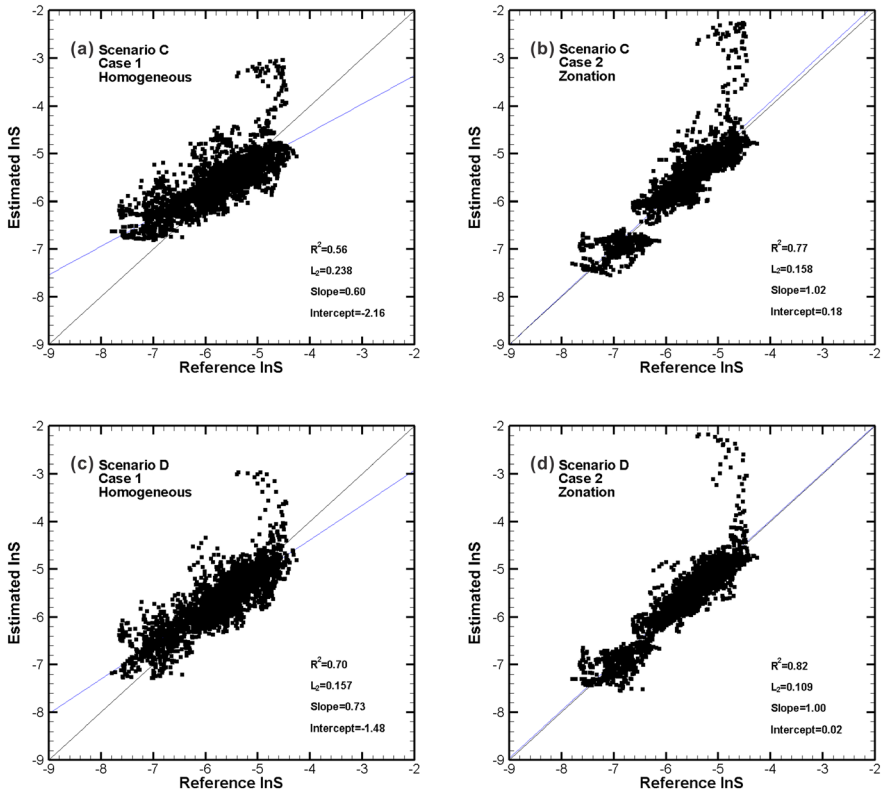

Figure 11. Scatterplots of reference versus estimated values of the storativity for (a) Scenario C (transient simultaneous pumping event), Case 1 (homogeneous prior); (b) Scenario C, Case 2 (zonal prior); (c) Scenario D (transient HT), Case 1; and (d) Scenario D, Case 2.

5. Summary and Conclusions

In this study, we first reiterate the importance of boundary and initial conditions for forward and inverse modeling of groundwater problems, as emphasized in Yeh et al. (2015). Then, we hypothesized that a simulation domain, larger than the groundwater basin's actual size and bounded by a constant head boundary, can be used with the HT survey to map the anomalously high and low T and S regions. These anomalously high and low T and S regions could delineate the groundwater basin's constant head or impermeable boundaries. Once the boundary conditions are identified, HT can estimate detailed T or T/S distributions.

Then, we conducted numerical experiments based on groundwater exploitation reduction in a pilot area of groundwater overexploitation control in the NCP to test our hypotheses. We used the large square domain and data from simultaneous pumping tests and HT tests under steady-state and transient flow situations to identify anomalously high/low-permeability zones around the groundwater basin. Groundwater basin boundaries close to anomalously high-permeability zones were assigned as constant head boundaries, while those with anomalously low-permeability zones were prescribed as impermeable boundaries. Groundwater flow fields interpolated and extrapolated from the observation data were subsequently used to determine the possible values for constant head boundaries. Using these identified boundaries, we assessed the effectiveness of uniform and zone prior information about T/S fields for simultaneous and HT inverse modeling approaches under steady-state and transient-state flow conditions.

The results of steady-state and transient-state experiments demonstrate the validity of our hypotheses. That is, for situations where the actual groundwater basin boundary conditions are unknown, using anomalously high and low T/S zones in the large square domain, we can define constant and impermeable boundaries for the basin. The numerical results also signify the advantages of HT surveys over multiple simultaneous pumping tests in capturing groundwater basins' true boundary conditions and in producing a higher-resolution characterization of subsurface heterogeneity. These results corroborate that HT surveys collect nonredundant information (Wen et al., 2020), critical for inverse modeling of groundwater problems.

We believe that this approach's logic applies to situations where the geometric shapes of groundwater basins are defined, but the types of boundaries are unknown. In these situations, we recommend some constant head conditions for these boundaries and use HT surveys to scan the entire basin. Resulting anomalously high and low T and T/S near the boundaries could suggest the types of boundary conditions for further numerical modeling purposes.

Besides, this study confirms that a reliable geology zonation map improves HT parameter estimations. However, such confirmation rests upon our assumption of perfect knowledge of the geology zone shape, distribution, and the mean T and S of each geologic zone. In real-world situations, detailed geologic investigations (Z. Zhao et al., 2016), in conjunction with dense geophysical surveys, are needed to reduce the uncertainty associated with these assumptions. Therefore, the general stochastic framework for incorporating geologic information (Zha et al., 2019) appears to be a viable approach for this purpose.

Although the application of this proposed approach to identifying real-world basin-scale aquifer boundary conditions remains to be tested, we believe that this study paves the way for developing a new generation of high-resolution aquifer characterization technology.

Data Availability Statement

The data used in this study can be downloaded from the link (https://doi.org/10.5281/zenodo.4070622).

Acknowledgments
This research was supported by the National Natural Science Foundation of China (Grant No. 41901039) and the China Scholarship Council (Grant No. 201808130026). T.-C. Jim Yeh also acknowledges the partial support by the U.S. NSF grant EAR1931756. We thank the Editors and three anonymous reviewers for their constructive comments.

References

Berg, S. J., & Illman, W. A. (2011). Three-dimensional transient hydraulic tomography in a highly heterogeneous glaciofluvial aquifer-aquitard system. *Water Resources Research*, *47*, W10507. https://doi.org/10.1029/2011WR010616

Bohling, G. C., Butler, J. J., Zhan, X., & Knoll, M. D. (2007). A field assessment of the value of steady shape hydraulic tomography for characterization of aquifer heterogeneities. *Water Resources Research*, *43*, W05430. https://doi.org/10.1029/2006WR004932

Cao, G., Zheng, C., Scanlon, B. R., Liu, J., & Li, W. (2013). Use of flow modeling to assess sustainability of groundwater resources in the North China Plain. *Water Resources Research*, *49*, 159–175. https://doi.org/10.1029/2012WR011899

Cardiff, M., Barrash, W., Kitanidis, P. K., Malama, B., Revil, A., Straface, S., & Rizzo, E. (2009). A potential-based inversion of unconfined steady-state hydraulic tomography. *Groundwater*, *47*(2), 259–270. https://doi.org/10.1111/j.1745-6584.2008.00541.x

Cardiff, M., Zhou, Y., Barrash, W., & Kitanidis, P. K. (2020). Aquifer imaging with oscillatory hydraulic tomography: Application at the field scale. *Groundwater*, *58*, 710–722. https://doi.org/10.1111/gwat.12960

Carrera, J., & Neuman, S. P. (1986). Estimation of aquifer parameters under transient and steady state conditions: 1. Maximum likelihood method incorporating prior information. *Water Resources Research*, *22*(2), 199–210. https://doi.org/10.1029/WR022i002p00199

Dafflon, B., Barrash, W., Cardiff, M., & Johnson, T. C. (2011). Hydrological parameter estimations from a conservative tracer test with variable-density effects at the Boise Hydrogeophysical Research Site. *Water Resources Research*, *47*, W12513. https://doi.org/10.1029/2011WR010789

Dagan, G. (2012). *Flow and transport in porous formations*. Berlin, Heidelberg: Springer Science & Business Media.

Daranond, K., Yeh, T.-C. J., Hao, Y., Wen, J.-C., & Wang, W. (2020). Identification of groundwater basin shape and boundary using hydraulic tomography. *Journal of Hydrology*, *588*, 125099. https://doi.org/10.1016/j.jhydrol.2020.125099

Freeze, R. A., & Cherry, J. A. (1979). *Groundwater: Englewood Cliffs*. New Jersey: Prentice-Hall Inc.

Gutjahr, A. L. (1989). Fast Fourier transforms for random field generation: Project report for Los Alamos Grant to New Mexico Tech. New Mexico Institute of Mining and Technology, Socorro.

Illman, W. A., Liu, X., & Craig, A. (2007). Steady-state hydraulic tomography in a laboratory aquifer with deterministic heterogeneity: Multi-method and multiscale validation of hydraulic conductivity tomograms. *Journal of Hydrology*, *341*(3–4), 222–234. https://doi.org/10.1016/j.jhydrol.2007.05.011

Illman, W. A., Liu, X., Takeuchi, S., Yeh, T.-C. J., Ando, K., & Saegusa, H. (2009). Hydraulic tomography in fractured granite: Mizunami Underground Research site, Japan. *Water Resources Research*, *45*, W01406. https://doi.org/10.1029/2007WR006715

Irsa, J., & Zhang, Y. (2012). A direct method of parameter estimation for steady state flow in heterogeneous aquifers with unknown boundary conditions. *Water Resources Research*, *48*, W09526. https://doi.org/10.1029/2011WR011756

Jiao, J., & Zhang, Y. (2014). Two-dimensional physical-based inversion of confined and unconfined aquifers under unknown boundary conditions. *Advances in Water Resources*, *65*, 43–57. https://doi.org/10.1016/j.advwatres.2013.10.011

Liu, F., Song, X., Yang, L., Han, D., Zhang, Y., Ma, Y., & Bu, H. (2018). Predicting the impact of heavy groundwater pumping on groundwater and ecological environment in the Subei Lake basin, Ordos energy base, Northwestern China. *Hydrology Research*, *49*(4), 1156–1171. https://doi.org/10.2166/nh.2017.281

Liu, F., Yeh, T.-C. J., Wang, Y.-L., Hao, Y., Wen, J.-C., & Wang, W. (2020). Characterization of basin-scale aquifer heterogeneity using transient hydraulic tomography with aquifer responses induced by groundwater exploitation reduction. *Journal of Hydrology*, *588*, 125137. https://doi.org/10.1016/j.jhydrol.2020.125137

Liu, H.-J., Hsu, N.-S., & Lee, T. H. (2009). Simultaneous identification of parameter, initial condition, and boundary condition in groundwater modelling. *Hydrological Processes*, *23*(16), 2358–2367. https://doi.org/10.1002/hyp.7344

Luo, N., Zhao, Z., Illman, W. A., & Berg, S. J. (2017). Comparative study of transient hydraulic tomography with varying parameterizations and zonations: Laboratory sandbox investigation. *Journal of Hydrology*, *554*, 758–779. https://doi.org/10.1016/j.jhydrol.2017.09.045

Mao, D., Yeh, T.-C. J., Wan, L., Hsu, K.-C., Lee, C.-H., & Wen, J.-C. (2013). Necessary conditions for inverse modeling of flow through variably saturated porous media. *Advances in Water Resources*, *52*, 50–61. https://doi.org/10.1016/j.advwatres.2012.08.001

Mohammadi, Z., & Illman, W. A. (2019). Detection of karst conduit patterns via hydraulic tomography: A synthetic inverse modeling study. *Journal of Hydrology*, *572*, 131–147. https://doi.org/10.1016/j.jhydrol.2019.02.044

Priestley, M. B. (1981). Spectral analysis and time series: Probability and mathematical statistics.

Pujol, J. (2007). The solution of nonlinear inverse problems and the Levenberg-Marquardt method. *Geophysics*, *72*(4), W1–W16. https://doi.org/10.1190/1.2732552

Schöniger, A., Nowak, W., & Hendricks Franssen, H.-J. (2012). Parameter estimation by ensemble Kalman filters with transformed data: Approach and application to hydraulic tomography. *Water Resources Research*, *48*, W04502. https://doi.org/10.1029/2011WR010462

Straface, S., Yeh, T.-C. J., Zhu, J., Troisi, S., & Lee, C. H. (2007). Sequential aquifer tests at a well field, Montalto Uffugo Scalo, Italy. *Water Resources Research*, *43*, W07432. https://doi.org/10.1029/2006WR005287

Sun, R., Yeh, T.-C. J., Mao, D., Jin, M., Lu, W., & Hao, Y. (2013). A temporal sampling strategy for hydraulic tomography analysis. *Water Resources Research*, *49*, 3881–3896. https://doi.org/10.1002/wrcr.20337

Walton, W. C. (1970). *Groundwater resource evaluation*. New York: McGraw-Hill.

Wang, B. (2011). Study on comprehensive quality assessment and coupling-coordination relationship of water-land resources in Heilonggang District. Chinese Academy of Geological Sciences. (in Chinese).

Wang, Y.-L., Yeh, T.-C. J., Wen, J.-C., Gao, X., Zhang, Z., & Huang, S.-Y. (2019). Resolution and ergodicity issues of river stage tomography with different excitations. *Water Resources Research*, *55*, 4974–4993. https://doi.org/10.1029/2018WR023204

Wei, R. (2018). *Evaluation of groundwater resources in plain area of Zhangwei River basin and relationship between surface water and groundwater conversion in typical section*. Beijing: China University of Geosciences (Beijing). (in Chinese)

Wen, J.-C., Chen, J.-L., Yeh, T.-C. J., Wang, Y.-L., Huang, S.-Y., Tian, Z., & Yu, C.-Y. (2020). Redundant and nonredundant information for model calibration or hydraulic tomography. *Groundwater*, *58*, 79–92. https://doi.org/10.1111/gwat.12879

Xiang, J., Yeh, T.-C. J., Lee, C.-H., Hsu, K.-C., & Wen, J.-C. (2009). A simultaneous successive linear estimator and a guide for hydraulic tomography analysis. *Water Resources Research*, *45*, W02432. https://doi.org/10.1029/2008WR007180

Yeh, T.-C. J. (1992). Stochastic modelling of groundwater flow and solute transport in aquifers. *Hydrological Processes*, *6*(4), 369–395. https://doi.org/10.1002/hyp.3360060402

Yeh, T.-C. J., & Liu, S. (2000). Hydraulic tomography: Development of a new aquifer test method. *Water Resources Research*, *36*(8), 2095–2105. https://doi.org/10.1029/2000WR900114

Yeh, T.-C. J., Mao, D.-Q., Zha, Y.-Y., Wen, J.-C., Wan, L., Hsu, K.-C., & Lee, C.-H. (2015). Uniqueness, scale, and resolution issues in groundwater model parameter identification. *Water Science and Engineering*, *8*, 175–194. https://doi.org/10.1016/j.wse.2015.08.002

Yeh, T.-C. J., Srivastava, R., Guzman, A., & Harter, T. (1993). A numerical model for water flow and chemical transport in variably saturated porous media. *Groundwater*, *31*(4), 634–644. https://doi.org/10.1111/j.1745-6584.1993.tb00597.x

Zha, Y., Yeh, T.-C. J., Illman, W. A., Mok, C. M. W., Tso, C.-H. M., Carrera, B. A., & Wang, Y.-L. (2019). Exploitation of pump-and-treat remediation systems for characterization of hydraulic heterogeneity. *Journal of Hydrology*, *573*, 324–340. https://doi.org/10.1016/j.jhydrol.2019.03.089

Zha, Y., Yeh, T. C. J., Illman, W. A., Tanaka, T., Bruines, P., Onoe, H., et al. (2016). An application of hydraulic tomography to a large-scale fractured granite site, Mizunami, Japan. *Ground Water*, *54*, 793–804. https://doi.org/10.1111/gwat.12421

Zha, Y., Yeh, T.-C. J., Mao, D., Yang, J., & Lu, W. (2014). Usefulness of flux measurements during hydraulic tomographic survey for mapping hydraulic conductivity distribution in a fractured medium. *Advances in Water Resources*, *71*, 162–176. https://doi.org/10.1016/j.advwatres.2014.06.008

Zhang, Y., Irsa, J., & Jiao, J. (2014). Three-dimensional aquifer inversion under unknown boundary conditions. *Journal of Hydrology*, *509*, 416–429. https://doi.org/10.1016/j.jhydrol.2013.11.024

Zhao, Y., Zhu, Y., Lin, Z., Wang, J., He, G., Li, H., et al. (2017). Energy reduction effect of the South-to-North Water Diversion Project in China. *Scientific Reports*, *7*, 15956. https://doi.org/10.1038/s41598-017-16157-z

Zhao, Z., & Illman, W. A. (2018). Three-dimensional imaging of aquifer and aquitard heterogeneity via transient hydraulic tomography at a highly heterogeneous field site. *Journal of Hydrology*, *559*, 392–410. https://doi.org/10.1016/j.jhydrol.2018.02.024

Zhao, Z., Illman, W. A., & Berg, S. J. (2016). On the importance of geological data for hydraulic tomography analysis: Laboratory sandbox study. *Journal of Hydrology*, *542*, 156–171. https://doi.org/10.1016/j.jhydrol.2016.08.061

Zhu, J., & Yeh, T.-C. J. (2005). Characterization of aquifer heterogeneity using transient hydraulic tomography. *Water Resources Research*, *41*, W07028. https://doi.org/10.1029/2004WR003790